Geophysical Research Letters

RESEARCH LETTER
10.1029/2021GL096923

Possible Control of Earth's Boron Budget by Metallic Iron

Liang Yuan[1] and **Gerd Steinle-Neumann**[1]

[1]Bayerisches Geoinstitut, Universität Bayreuth, Bayreuth, Germany

Key Points:

- Using density functional theory calculations we show that boron behavior changes from lithophile to siderophile at deep mantle conditions
- Liquid silicate is enriched in the heavier boron isotope by ~1‰ relative to liquid metal at high pressure and temperature
- High boron contents in deep diamonds and isotopically light boron in oceanic hotspots may reflect contributions from metallic reservoirs

Supporting Information:

Supporting Information may be found in the online version of this article.

Correspondence to:

L. Yuan,
liang.yuan@uni-bayreuth.de

Citation:

Yuan, L., & Steinle-Neumann, G. (2022). Possible control of Earth's boron budget by metallic iron. *Geophysical Research Letters*, *49*, e2021GL096923. https://doi.org/10.1029/2021GL096923

Received 3 DEC 2021
Accepted 2 MAY 2022

Abstract Boron is considered a principal tracer for crustal recycling into the depleted mantle, and high boron anomalies and isotopically light boron (^{10}B) in mantle-derived samples have been interpreted as the result of subduction. Using density functional theory, we predict that boron behavior changes from lithophile to siderophile, with the calculated boron partition coefficients ($D^{m/s}$) between liquid metal and silicate ranging from $\log_{10}D^{m/s} \leq -0.8$ at low pressure–temperature conditions (10 GPa, 3000 K) to $\log_{10}D^{m/s} \geq 3.7$ at high pressure and temperature (130 GPa, 5000 K). We further predict that the silicate becomes enriched in the heavier boron isotope (^{11}B) by >1‰ relative to metal at high pressure–temperature. Our results suggest that Earth's core may hold >50% of Earth's boron budget and that a high boron content in deep diamonds and isotopically light boron in ocean islands basalts may reflect contributions from metallic reservoirs, rather than being attributed to crustal subduction and recycling.

Plain Language Summary Plate tectonics promotes the transport of surface rocks into the mantle, producing much of its chemical heterogeneity. Boron, a quintessential crustal element, is often used as a proxy for crustal contributions when found in mantle rocks and is, therefore, one of the central tools in geochemistry to trace recycling/mixing in the mantle. Using quantum mechanical calculations, we find that the chemical behavior of boron changes from lithophile (rock-loving) to siderophile (iron-loving) under pressure–temperature conditions relevant to core formation. Thus, much boron may have been transported to the core, and the core may be Earth's largest boron reservoir, rather than the crust. Chemical heterogeneity in the mantle inferred from boron signatures could therefore also result from chemical exchange between the core and mantle or equilibration with metallic iron dispersed throughout the mantle.

1. Introduction

Boron (B) is an incompatible, lithophile element (Ottolini et al., 2009), depleted in the upper mantle (<0.2 μg/g) (Marschall et al., 2017) and enriched in the oceanic crust by orders of magnitude (up to 200 μg/g) (Leeman & Sisson, 1996). At the same time, its two isotopes, ^{11}B and ^{10}B, are highly fractionated in geological reservoirs ($\delta^{11}B = (^{11}B/^{10}B)_{sample}/(^{11}B/^{10}B)_{standard} - 1$, values given in ‰) with, for example, average compositions of $\delta^{11}B = +39.6$‰ in seawater, and $\delta^{11}B = -7.1$‰ in mantle-derived rocks (Palmer, 2017). Boron is thus often used as a tracer of recycled crust in the mantle (De Hoog & Savov, 2018) because minor additions strongly alter its B signature.

Due to its scarcity in the deep Earth, the origin of boron in mantle-derived samples, most prominently in blue Type IIb diamonds with up to 8 μg/g B (Gaillou et al., 2012; Smith et al., 2018), has been linked to subduction (Smith et al., 2018). However, a recent petrographic study showing that naturally occurring titanium diboride (TiB_2) crystallizes predominantly from metallic melts at low oxygen fugacity (f_{O_2}) (Griffin et al., 2020) suggests that metals can exert control on Earth's boron distribution given that low f_{O_2} likely governed core formation (Rubie et al., 2011). As metallic iron is present predominantly in the core and likely at percent level throughout the mantle (Frost et al., 2004), its impact on Earth's boron budget merits consideration.

Some ocean island basalts (OIB) with deep origin show isotopically lighter δ^{11}B (as low as −20.7‰) than depleted mantle, which has been interpreted as a signature of recycled slab material that is successively stripped of boron and becomes isotopically lighter during dehydration (Walowski et al., 2019, 2021). However, other aspects of OIB geochemistry appear to require a core contribution (Brandon et al., 1998; Herzberg et al., 2013; Humayun, 2004; Rizo et al., 2019), with low ^{182}W/^{184}W reported for Icelandic lavas (Mundl-Petermeier et al., 2020) the most significant example; ocean island basalts (OIB) δ^{11}B may be influenced in a similar fashion.

To establish boron composition of Earth's core, its metal–silicate partitioning at high pressure–temperature (*P*–*T*) conditions during core formation must be known. Measuring boron in samples recovered from high *P*–*T*

experiments, however, presents significant challenges (Bourdon et al., 2018), which have prevented such studies. Here, we perform density functional theory (DFT) molecular dynamics (MD) simulations with boron in metallic and silicate melts to determine partitioning and isotope fractionation at 10–130 GPa and 3000–5000 K, covering P–T conditions of core differentiation (Siebert et al., 2012). We consider partitioning of elemental B and B_2O_3, reflecting reduced and oxidized magma ocean conditions, and integrate the results in core formation models (Rudge et al., 2010).

2. Computational Methods

2.1. Density Functional Theory Molecular Dynamics Simulations

We perform electronic structure calculations based on Kohn-Sham (KS) density functional theory (DFT) to obtain internal energy, Hellmann-Feynman stresses and forces with a plane wave approach (with an energy cutoff of 450 eV), and periodic boundary conditions using the Vienna ab initio simulation package (VASP) (Kresse & Furthmüller, 1996). We use the projector augmented wave implementation and atomic files (Kresse & Joubert, 1999) in the generalized gradient approximation to exchange and correlation (Perdew et al., 1996). Electronic KS-density functional theory (DFT) states are calculated at the Brillouin zone center. Molecular dynamics (MD) simulations are performed in the N–V–T ensemble, where the number of atoms (N) and the volume (V) of the cell are kept fixed, and T is controlled by a Nosé-Hoover thermostat. After convergence of the electronic cycle, atoms are advanced with a time step of $\Delta t = 1.0$ fs along the Hellmann-Feynman forces.

2.2. Partition Coefficient

We use two-phase simulations to model partitioning directly, mimicking an experiment by putting metallic and silicate phases in direct contact in a simulation cell and tracking the distribution of boron atoms as the system reaches equilibrium, providing a semi-quantitative understanding.

The partition coefficient of a solute ($D_{\mathrm{solu}}^{\mathrm{m/s}}$, the ratio of molar fractions of the solute, B or B_2O_3, in the solvents Fe metal and $MgSiO_3$ silicate) is quantitively determined by the chemical equilibrium between them,

$$\mu_{\mathrm{solu}}^{\mathrm{m}}\left(P, T, c_{\mathrm{solu}}^{\mathrm{m}}\right) = \mu_{\mathrm{solu}}^{\mathrm{s}}\left(P, T, c_{\mathrm{solu}}^{\mathrm{s}}\right), \tag{1}$$

where μ_{solu} and c_{solu} are the chemical potential and mole fraction of solute in metallic Fe and silicate $MgSiO_3$ liquids (denoted by superscripts "m" and "s", respectively). As the chemical potential μ_{solu} diverges logarithmically in the low-concentration limit, it is useful to express μ_{solu} at P–T as

$$\mu_{\mathrm{solu}} = k_{\mathrm{B}}T \ln c_{\mathrm{solu}} + \mu_{\mathrm{solu}}^{\dagger} + \lambda_{\mathrm{solu}} c_{\mathrm{solu}} + O\left(c_{\mathrm{solu}}^2\right), \tag{2}$$

and following previous studies (Alfè et al., 2002), we neglect terms $O\left(c_{\mathrm{solu}}^2\right)$ and higher. Therefore, only $\mu_{\mathrm{solu}}^{\dagger}$ and λ_{solu} must be determined in the calculations, with

$$\mu_{\mathrm{solu}} = k_{\mathrm{B}}T \ln c_{\mathrm{solu}} + \mu_{\mathrm{solu}}^{\dagger} + \lambda_{\mathrm{solu}} c_{\mathrm{solu}} \tag{3}$$

for the the solute (i.e., B or B_2O_3), and

$$\mu_{\mathrm{solv}} = \mu_{\mathrm{solv}}^{0} + \left(k_{\mathrm{B}}T + \lambda_{\mathrm{solu}}\right) \ln\left(1 - c_{\mathrm{solu}}\right) + \lambda_{\mathrm{solu}} c_{\mathrm{solu}} \tag{4}$$

for the solvent (i.e., Fe or $MgSiO_3$), where μ_{solv}^{0} is the chemical potential of the pure solvent. Gibbs energy (G) of solution can then be expressed by

$$\begin{aligned} G &= N_{\mathrm{solu}}\mu_{\mathrm{solu}} + N_{\mathrm{solv}}\mu_{\mathrm{solv}} \\ &= N\left[c_{\mathrm{solu}}\mu_{\mathrm{solu}} + \left(1 - c_{\mathrm{solu}}\right)\mu_{\mathrm{solv}}\right] \\ &= N\left\{c_{\mathrm{solu}}\left[k_{\mathrm{B}}T \ln c_{\mathrm{solu}} + \mu_{\mathrm{solu}}^{\dagger} + \lambda_{\mathrm{solu}} c_{\mathrm{solu}}\right] + \right. \\ &\quad \left.\left(1 - c_{\mathrm{solu}}\right)\left[\mu_{\mathrm{solv}}^{0} + \left(k_{\mathrm{B}}T + \lambda_{\mathrm{solu}}\right) \ln\left(1 - c_{\mathrm{solu}}\right) + \lambda_{\mathrm{solu}} c_{\mathrm{solu}}\right]\right\}, \end{aligned} \tag{5}$$

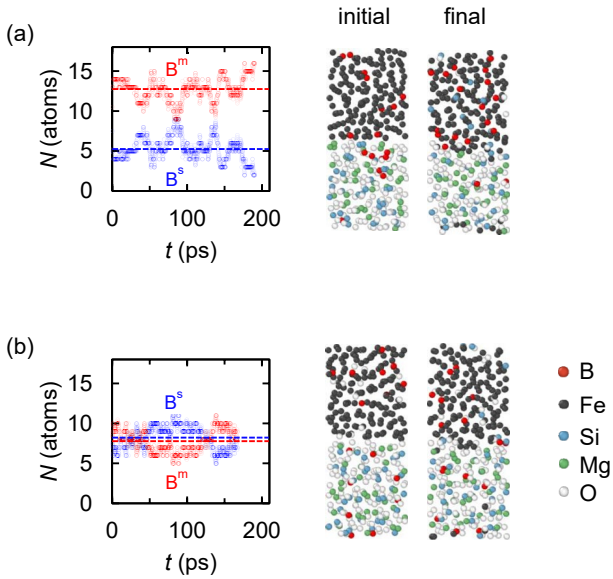

Figure 1. Results from two-phase DFT-MD simulation. (left) Time-evolution of the number (N) of boron atoms in the silicate (B^s) and metallic (B^m) liquids for $Fe_{150}B_9$–$Mg_{35}Si_{35}O_{105}B_9$ at 43.0 ± 0.2 GPa and (a) 3494 K, and for $Fe_{150}B_8O_{12}$–$Mg_{35}Si_{35}O_{117}B_8$ at 40.3 ± 0.2 GPa and (b) 3493 K. Horizontal dashed lines indicate the mean N over the whole trajectory. (right) Initial and final configurations of the simulations. Detailed P–T conditions of the simulation are given in Table S2 of Supporting Information S1, and animations showing the development of the simulation cell are provided in Movie S1.

where N_{solu} and N_{solv} are the number formula units of solutes and solvents, respectively, and $N = N_{solu} + N_{solv}$. As standard DFT-molecular dynamics (MD) simulations do not provide entropy of the system, we compute the Helmholtz energy (A) by thermodynamic integration from an ideal gas (reference system with A_{IG}) to the KS-DFT system (target system with A_{DFT}) at fixed V and T, employing a coupling constant χ (Dorner et al., 2018),

$$\Delta A = A_{DFT} - A_{IG} = \int_0^1 \left\langle \frac{\partial U_\chi}{\partial \chi} \right\rangle_{U_\chi} d\chi, \tag{6}$$

where $\left\langle \frac{\partial U_\chi}{\partial \chi} \right\rangle_{U_\chi}$ is the thermodynamic average of quantity $\partial U_\chi/\partial\chi$ over an ensemble generated by the Hamiltonian for which

$$U\chi = (1 - \chi)U_{IG} + \chi U_{DFT}. \tag{7}$$

With A_{DFT} determined, G can be calculated by $G = A + PV$. The equation of state for each liquid composition calibrates calculations to constant P,

$$G(P_2, T) - G(P_1, T) = \left(\int_{P_1}^{P_2} V\, dP \right)_T. \tag{8}$$

With G calculated at several solute concentrations and P–T, we can regress values of $\mu^\dagger_{solu}$ and λ_{solu} (Equation 5); μ_{solu} and μ_{solv} can then be obtained for the silicate and metal separately (Equations 3 and 4). Finally, the equilibrium partition coefficient is calculated as $D^{m/s}_{solu} = c^m_{solu}/c^s_{solu}$.

2.3. Equilibrium Isotope Fractionation

To evaluate whether core–mantle segregation/interaction yields a boron isotope difference between these reservoirs, we compute equilibrium isotope fractionation factors between metallic and silicate melts, expressed as $1000 \cdot \ln(\alpha^{m/s})$, where $\alpha^{m/s}$ for boron is obtained from the reduced partition function ratio (β) in metal (β^m) and silicate (β^s),

$$\alpha^{m/s} = \beta^m/\beta^s. \tag{9}$$

We calculate β for the liquids based on the single-atom approximation (Kowalski & Jahn, 2011),

$$\beta = 1 + \left(\frac{1}{m_l} - \frac{1}{m_h} \right) \frac{\hbar^2}{8k_B^2 T^2} \langle F \rangle, \tag{10}$$

where F is the force constant acting on the atom with the light (mass m_l) and heavy (mass m_h) isotope, $\hbar$ is the reduced Planck and k_B Boltzmann's constant. The use of Equation 10 requires that vibrational frequencies ω (cm^{-1}) $\leq 1.39\,T$ related to the element of interest (Kowalski & Jahn, 2011). This is valid for high T explored in this study as $\omega > 4000$ cm^{-1} are only plausible in hydrogen-bearing compositions. Further details and some analyses of the results are included in the Supporting Information S1.

3. Results

3.1. Boron Metal–Silicate Partitioning

Two-phase simulations are designed with liquid metal (Fe_{150}) and silicate ($Mg_{35}Si_{35}O_{105}$) cells put together (Figure S1 in Supporting Information S1), both initially containing equal numbers of boron atoms (B^m and B^s denote boron atoms in metal and silicate, respectively). From the time-evolution of the boron distribution at ~40 GPa and ~3500 K, we observe strong boron partitioning into the metal, with $B^m/B^s = 2.43 \pm 0.02$ (Figure 1a; Movie S1).

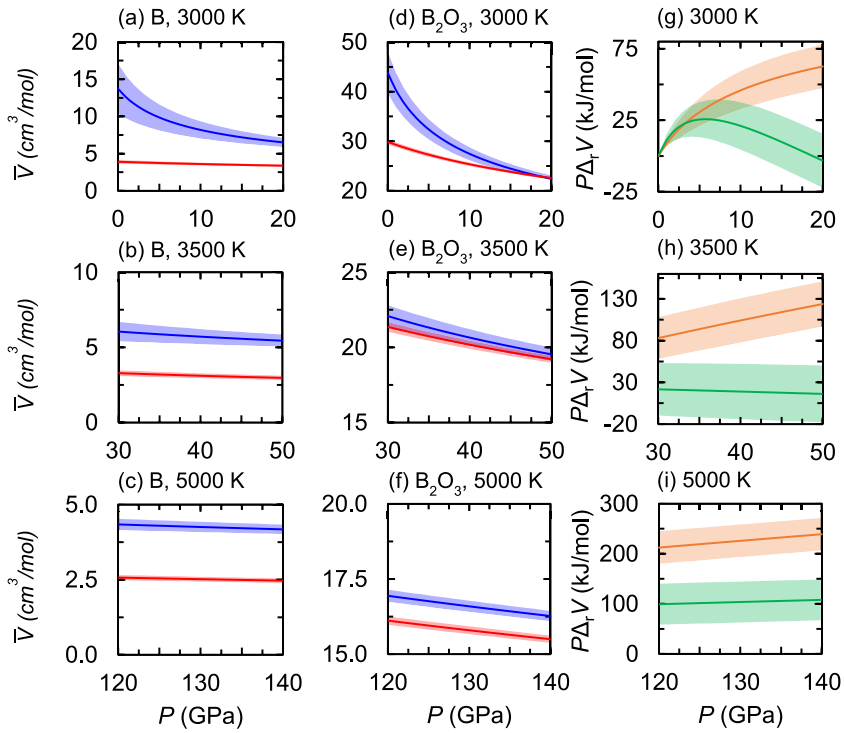

Figure 2. Partial molar volume ($\overline{V}$) and $P\Delta_r\overline{V}$ energetic contribution to Gibbs energy change associated with boron transfer from metal to silicate. $\overline{V}$ of B (a–c) and B_2O_3 in silicate (blue) and iron (red) melts (d–f), and $P\Delta_r\overline{V}$ terms associated with B (orange) and B_2O_3 (green) transfer from metal to silicate (g–i). Pressure–volume (P–V) relationships and local second-order Birch–Murnaghan equations of state for silicate and metal are constructed from DFT-MD simulations with different B and B_2O_3 contents (c) of 0.0, 6.3, 11.8, 16.7, 21.1 mol% for $(MgSiO_3)_{1-c}B_c$ and $(MgSiO_3)_{1-c}(B_2O_3)_c$, 0.0, 2.0, 3.8, 7.4, 12.3 mol% for $Fe_{1-c}B_c$, and 0.0, 2.0, 3.8, 5.7, 7.4 mol% for $Fe_{1-c}(B_2O_3)_c$ (*cf.* Figures S5 and S6; Tables S3 and S4 in Supporting Information S1). Shaded areas represent uncertainties propagated from the standard error of mean P from DFT-MD simulations.

Additional two-phase simulations reveal lithophile behavior of B at low P (~10 GPa) ($B^m/B^s = 0.79 \pm 0.01$) (Figure S2a in Supporting Information S1), while the siderophile nature of B observed at ~40 GPa persists to ~130 GPa, with enhanced $B^m/B^s = 5.19 \pm 0.05$ (Figure S2b in Supporting Information S1). When more oxygen is available in the form of B_2O_3, B^m is slightly smaller than B^s ($B^m/B^s = 0.95 \pm 0.01$) at ~40 GPa (Figure 1b and Movie S1 in Supporting Information S1), suggesting lower boron compatibility in the metal under more oxidizing conditions. Nevertheless, appreciable amounts of boron partition into the metal, more so than conventionally expected (see, e.g., review by Grew 2017; Shearer & Simon 2017).

As an equilibrium property, boron distribution between metal and silicate can be understood in terms of the Gibbs energy difference ($\Delta_r G$) of B incorporation. With $\Delta_r G = \Delta_r U + P\Delta_r\overline{V} - T\Delta_r S$ this involves three contributions (Wilson & Militzer, 2012): (a) a potential energy term $\Delta_r U$, (b) $P\Delta_r\overline{V}$ from the difference of partial molar volume ($\overline{V}$) of boron, and (c) an entropic term $-T\Delta_r S$. Among these, (b) is directly accessible from DFT-MD simulations, which provides insight into a critical aspect of the underlying processes. We compute $\overline{V}$ of B dissolved in the metal ($\overline{V}^m_B$) considering different $Fe_{1-c}B_c$ compositions, and in the silicate ($\overline{V}^s_B$) for $(MgSiO_3)_{1-c}B_c$ compositions (for $\overline{V}^m_{B_2O_3}$ correspondingly). We find $\overline{V}^s > \overline{V}^m$ for both B and B_2O_3 at all P–T conditions considered (Figure 2), that is, $\Delta_r\overline{V} > 0$. At low P (0–20 GPa), $\overline{V}^s_B$ is highly compressible and $\overline{V}^m_B$ remains essentially constant, leading to a rapid decrease in $\Delta_r\overline{V}$. Similarly, $\overline{V}^s_{B_2O_3} > \overline{V}^m_{B_2O_3}$ at 0 GPa, but they become comparable at 20 GPa. $\Delta_r\overline{V}$ for boron varies little in the higher-P range, with $\overline{V}^s_B$ significantly larger than $\overline{V}^m_B$, and $\overline{V}^s_{B_2O_3}$ similar to $\overline{V}^m_{B_2O_3}$. The $P\Delta_r\overline{V}$ term increasingly favors boron dissolution in metal with P, much more strongly for B than for B_2O_3.

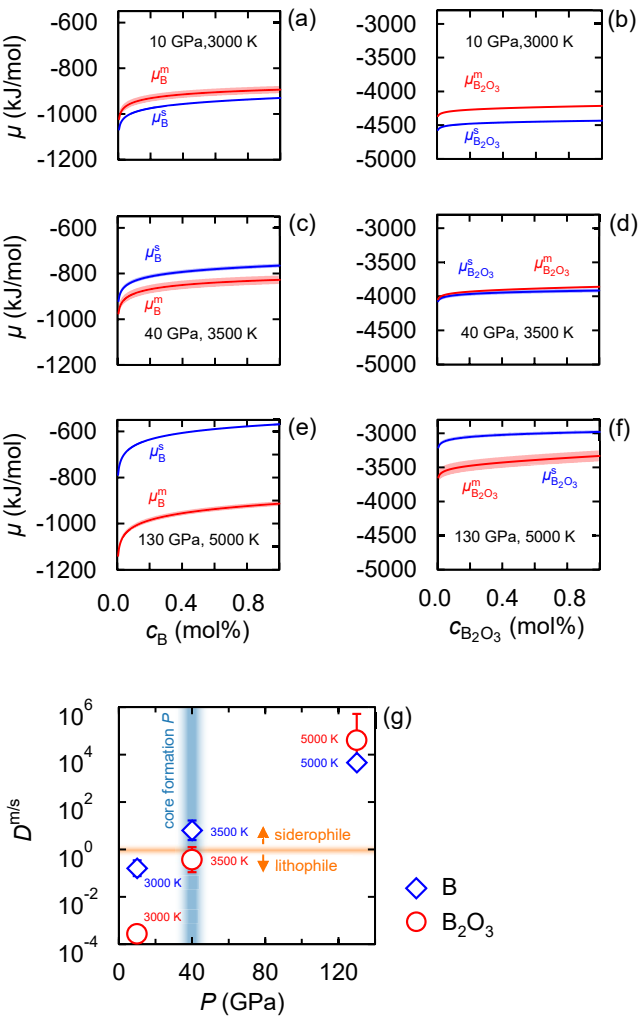

Figure 3. Chemical potentials (μ) and partitioning coefficients of boron between iron and silicate melts ($D^{m/s}$). μ of B (a, c, e) and B_2O_3 (b, d, f) in silicate (blue) and iron (red) as a function of boron content, $c_{B(\text{or } B_2O_3)}$ in mol% at three different P–T conditions. $D^{m/s}$ (on a log scale) as a function of P determined by equal μ in each phase (g). The vertical band (blue) shows the average P expected during core–mantle segregation (Siebert et al., 2012). For the low boron content in the mantle, $D^{m/s}$ remain essentially independent of concentration (cf., Figure S10 in Supporting Information S1).

To quantitatively address the energetics of boron exchange, we compute Gibbs energies $G(P, T, c)$ for B-bearing $MgSiO_3$ silicate and Fe liquids by thermodynamic integration at three P–T conditions relevant for core formation: 10 GPa and 3000 K, 40 GPa and 3500 K, and 130 GPa and 5000 K (Tables S4 and S5 in Supporting Information S1). We fit $G(P, T, c)$ results for four boron concentrations (c_B or $c_{B_2O_3}$) and the boron-free silicate and iron with a concentration-dependent expression (Equation 5; Figure S9 in Supporting Information S1) from which the chemical potentials of boron in silicate (μ_B^s) and metallic (μ_B^m) solutions are calculated (Equation 3; Figures 3a–3f): $\mu_B^s < \mu_B^m$ at 10 GPa, reflecting lithophile behavior; μ_B^s becomes larger than μ_B^m at higher P–T, indicating siderophile behavior, consistent with the results from the two-phase simulations. A similar transition from lithophile to siderophile is predicted for B_2O_3—with $\mu^s_{B_2O_3}$ substantially smaller than $\mu^m_{B_2O_3}$ at 10 GPa, slightly smaller at 40 GPa, but significantly larger at 130 GPa. From the chemical potentials, the boron metal–silicate partition coefficient $D_B^{m/s}$ can be readily calculated utilizing Equation 1 (Figure 3g): $\log_{10} D_B^{m/s}$ increases from -0.8 ± 0.3 at 10 GPa and 3000 K to 3.7 ± 0.1 at 130 GPa and 5000 K; for B_2O_3, $\log_{10} D^{m/s}_{B_2O_3}$ increases from -3.6 ± 0.4 to 4.6 ± 1.1 over the same conditions.

Both thermodynamic integration and two-phase simulations indicate that boron is lithophile at low P, but turns siderophile at high P. As no experiment has directly measured boron metal–silicate partitioning, a discussion must rely on indirect evidence. (a) Experimental charges, both silicate (Shahar et al., 2015) and iron liquids (Sokol et al., 2019) in boron nitride sample capsules, recovered from $P < 10$ GPa reveal boron incorporation, with concentrations in silicate (2–5 wt%) orders of magnitude larger than in Fe metal (500–800 μg/g). This qualitatively agrees with the lithophile character of boron from our low-P simulations. (b) At higher P, numerous iron borides (e.g., FeB_4, Fe_2B_7). have been predicted (Kolmogorov et al., 2010) or synthesized (Gou et al., 2013); the enhanced reactivity between iron and boron may reflect the transition from lithophile to siderophile behavior. Given our results and previous experimental observations that conventional highly lithophile elements partition strongly into Fe–S liquids over coexisting silicate melts at low f_{O_2} (e.g., Nb and Ta in Wood & Kiseeva, 2015, Ti in Kiseeva & Wood, 2015; Steenstra et al., 2020, and U in Wohlers & Wood, 2015), the chemical behavior of elements may strongly deviate from Goldschmidt's original classification at conditions of planetary formation and differentiation.

While our DFT-MD simulations are performed with the goal of first-order constraints on the lithophile and siderophile characteristics of boron on three P–T points (Figure 3 and S10 in Supporting Information S1), extrapolating $\log_{10} D_B^{m/s}$ for elemental B at 10 GPa to higher P tentatively puts the transition between lithophile and siderophile behavior at ~20 GPa. With metal saturation in the transition zone and below, our results suggest that the amount of boron in metallic reservoirs in the mantle can be significantly larger than that recycled into the lower mantle via subduction, particularly because dehydration at subarc depths (Chemia et al., 2015; Syracuse et al., 2010) leads to a removal of >99% boron from the slab crust during subduction (Marshall et al., 2022; McCaig et al., 2018).

3.2. Equilibrium Boron Isotope Fractionation

Previous experiments have demonstrated that metallic phases are depleted in heavy isotopes of light elements such as carbon (Satish-Kumar et al., 2011), silicon (Hin et al., 2014; Shahar et al., 2009), and nitrogen (Dalou et al., 2019) even at mantle T. As isotope fractionation arises from the influence of mass differences on vibrational energies in coexisting phases, and scales with $(m_h - m_l)/(m_h \cdot m_l)$ approximately (Equation 10) (Schauble, 2004),

metal–silicate equilibration is expected to fractionate boron isotopes more strongly than the heavier elements mentioned above. We estimate boron isotope fractionation based on configuration snapshots extracted from DFT-MD trajectories in $Fe_{50}B_1$ and $(MgSiO_3)_{15}B_1$ cells. Force constants acting on the boron atom in the silicate are 2–4 times larger than in the metal at all *P*–*T* conditions considered (Figures S11a–S11c in Supporting Information S1), leading to larger $\delta^{11}B$ values in silicate than coexisting metal. Assuming core–mantle segregation at 40 GPa and 3500 K (Siebert et al., 2012), the core would have smaller $\delta^{11}B$ by ~1‰. Fractionation is predicted to depend on *T*, but not on *P* (Figure S11d in Supporting Information S1). This difference should be resolvable in modern isotope measurements ($\delta^{11}B \pm 0.3$‰) (Foster et al., 2018).

4. Discussion

4.1. Earth's Boron Budget

Boron's siderophile behavior at high *P* indicates that core segregation should have stripped the silicate mantle of a large proportion of boron, and potentially accounts for >50% of Earth's boron inventory (see below). However, boron concentration in bulk silicate Earth (BSE) follows the volatility trend of lithophile elements relative to Ivuna-type (CI) chondrites (Lodders, 2003; Palme & O'Neill, 2013; Wood et al., 2019), a paradoxical situation that can have several possible causes:

1. Establishing volatile depletion requires information on the representative compositions of both bulk silicate Earth (BSE) and CI chondrites. Fresh mid-ocean ridge basalt (MORB) glasses have been used to derive the bulk silicate Earth (BSE) boron budget, with B compatibility during MORB extraction following that of praseodymium (Pr) (Marschall et al., 2017). Using the well-constrained Pr content of the depleted mantle and B/Pr ratios from MORB, Marschall et al. (2017) tightly constrain the B budget in the BSE to 0.19 μg/g. By contrast, the B content for CI chondrites is reported as 0.27–1.2 μg/g (Shaw et al., 1988; Zhai & Shaw, 1994; see also Marschall et al., 2017 and references therein), partly due to sample history and analytical challenges. This suggests a range of depletion factors, $f_B = (B/Mg)_{BSE}/(B/Mg)_{CI} = 0.07$–$0.30$, rather than a single value of $f_B \sim 0.10$ used, for example, by Wood et al. (2019).
2. The concept of condensation *T* for boron is problematic due to its nucleosynthesis. Unlike other elements, boron, together with lithium and beryllium, has a low nuclear binding energy (Prantzos, 2007). Production of boron is attributed primarily to spallation reactions between galactic cosmic rays (GCR, mainly composed of protons and α particles) and interstellar gas/dust nuclei (carbon, nitrogen, and oxygen) (Prantzos, 2012; Reeves et al., 1970). The inefficient nature of spallogenic nucleosynthesis leads to an abundance of B several orders of magnitude lower than that of the stable neighboring elements (helium and carbon) (Palme et al., 2013), and the resulting isotopic composition varies significantly depending on the energy of GCR (Cassé et al., 1995; Ramaty et al., 1996). The isotope heterogeneity is documented by $\delta^{11}B$ in chondrules spanning −50‰ to +50‰ (Chaussidon & Robert, 1995), which is too large to be controlled by mass-dependent fractionation through evaporation or condensation, but can be explained by presolar grains contributing anomalous $\delta^{11}B$. Boron condensation from the solar nebular gas at a unique *T* is therefore not a meaningful concept (Chaussidon & Robert, 1997; M. C. Liu & Chaussidon, 2018).
3. Alternatively, the boron budget in the BSE may have been replenished by boron-rich, late-accreted material after core–mantle differentiation. This late veneer scenario is supported by an excess of highly siderophile elements (HSEs: Os, Ir, Ru, Rh, Pt, Pd, Re, and Au) in the BSE and their ratios (e.g., Os/Ir) resembling those in carbonaceous chondrites (Chou, 1978), the abundance ratios (Wang & Becker, 2013) and isotopic compositions (Varas-Reus et al., 2019) of moderately volatile and chalcogen elements (S, Se, and Te), and would account for large portions of Earth's volatile budget, including boron. However, several studies (Hellmann et al., 2021; König et al., 2014; Yierpan et al., 2019) have argued that S–Se–Te compositions are subject to mantle fractionation processes (e.g., partial melting, metasomatic overprinting), such that peridotite samples (Varas-Reus et al., 2019; Wang & Becker, 2013) do not provide reliable proxies for the composition of the BSE. Recent studies based on nucleosynthetic isotope anomalies for the siderophile elements ruthenium and molybdenum (Bermingham & Walker, 2017; Fischer-Gödde & Kleine, 2017; Worsham & Kleine, 2021) are not prone to post-accretionary modifications and characterized late-accreted material as isotopically distinct from carbonaceous chondrites, but identical to enstatite chondrites originating from the inner solar system. These studies support a scenario of homogeneous accretion (Wood et al., 2010) and volatiles delivery to the Earth during the main phase of accretion and differentiation (Jin & Bose, 2019; Piani et al., 2020).

With a substantial amount of boron likely present during planetary differentiation, we explore two core formation scenarios to determine boron partitioning based on our predicted $D_B^{m/s}$ and $D_{B_2O_3}^{m/s}$. We consider a range of initial concentrations such that the resulting BSE content after core segregation is close to 0.19 μg/g (Marschall et al., 2017). Single-stage core formation at 40 GPa and 3500 K (Siebert et al., 2012), as a first-order approximation, yields a boron content in the core of 0.1–2.3 μg/g (i.e., 2.7–46 × 10^{17} kg), 1–18 times the crustal reservoir of ∼2.6 × 10^{17} kg (Marschall et al., 2017), with the large variation arising from the difference in partition coefficients $D_B^{m/s}$ and $D_{B_2O_3}^{m/s}$. Continuous core formation considers planetary accretion and differentiation as synchronous processes and accounts for accreting material heterogeneity and metal–silicate equilibrium over a wide *P*–*T* range during planetary growth. We follow the framework of Rudge et al. (2010) for the accretion of differentiated embryos: their cores partially re-equilibrate with the proto-Earth mantle, while the remainder is directly added to Earth's core (details in Supporting Information S1). In multiple sets of calculations, we find 0.7–6.2 μg/g in the core (i.e., 13–120 × 10^{17} kg), both larger values and a larger concentration range than from single-stage core formation.

4.2. Core Contributions to Anomalous $\delta^{11}B$ in Oceanic Hotspots

Isotopically light boron signatures in hotspot lavas have been broadly interpreted as sampling crustal boron in their sources (Walowski et al., 2019, 2021). This scenario is consistent with the standard view that (a) OIBs contain materials recycled from the surface of the Earth (Hofmann & White, 1982); (b) boron is exclusively hosted in the crust/seawater (De Hoog & Savov, 2018); and (c) the magnitude of equilibrium isotope fractionation – scaling with T^{-2} (Schauble, 2004) – is expected to be negligible at high *T* of the deep Earth. Our results provide evidence for previously unrecognized primordial boron reservoirs possibly enriched in ^{10}B in the deep mantle and core.

To explore potential core components in the mantle sources responsible for the isotopically light boron in OIB, we assemble a global set of OIB $\delta^{11}B$ data (Chaussidon & Marty, 1995; Hartley et al., 2021; Kobayashi et al., 2004; Marschall & Jackson, 2020; Walowski et al., 2021), together with $\mu^{182}W$ (deviation of $^{182}W/^{184}W$ from the terrestrial Alfa Aesar W standard in ppm) data (Jackson et al., 2020; Mundl-Petermeier et al., 2020) from nine volcanic hotspots (Table S8 in Supporting Information S1). Negative $\mu^{182}W$ anomalies have been traditionally used as fingerprints of the core (e.g., Rizo et al., 2019) and a correlation between $\delta^{11}B$ and $\mu^{182}W$ may support the core as a B reservoir. However, strong isotopic heterogeneity at regional/outcrop scales, with $\mu^{182}W$ in individual hotspots spanning >50% of the total variability of the mean (Figure S13 in Supporting Information S1), obscures any potential correlation between $\delta^{11}B$ and $\mu^{182}W$. Concurrent measurements of $\delta^{11}B$ and other geochemical indices (e.g., $\mu^{182}W$) in terrestrial rocks at smaller scales will be needed to assess whether, and to what extent, core formation elevated $\delta^{11}B$ of the BSE relative to chondrites, and whether OIBs entrain isotopically light B from the core.

4.3. Reappraisal of the Origin of Blue Diamonds

In addition to a high boron content, Type IIb diamonds are characterized by the presence of Fe and Fe-carbide inclusions (Smith et al., 2018) which potentially suggests that they grew from iron–carbon melts rather than the recycled crust. This diamond formation mechanism is supported by (a) the inference that up to 90% of Earth's carbon resides in metallic iron (Fischer et al., 2020); (b) several experiments strongly suggest that iron–carbon melts play a role both as a source and crystallization medium for diamond growth (Palyanov et al., 2013, 2020; Sokol et al., 2019). Notably, diamonds synthesized this way incorporate boron up to hundreds of μg/g (Sokol et al., 2019); (c) natural diamonds containing metallic inclusions suggest direct diamond precipitation from metallic liquids by carbon saturation (Smith et al., 2016) due to physical or chemical perturbations.

Rather than boron in Type IIb diamonds representing crustal recycling, its predicted siderophile nature suggests the fingerprint of a metallic reservoir. The Earth's core provides an unlimited source of metal, which may deliver boron through infiltration into the lowermost mantle (e.g., Bull et al., 2009). Such mechanism has been explored as the potential cause of the chemical diversity in OIBs, for example, low $^{182}W/^{184}W$ (Mundl-Petermeier et al., 2020), high $^{3}He/^{4}He$ (Bouhifd et al., 2013), $^{186}Os/^{188}Os$ (Brandon et al., 1998) and Fe/Mn ratios (Humayun, 2004). The hypothesis of a core contribution to the boron signature of Type IIb is highly conjectural as it

requires more than 2,000 km of vertical migration of dense core components with minimal dilution of boron signatures.

Alternatively, metallic Fe prevalent throughout the deep mantle (Frost & McCammon, 2008) offers a simple explanation for boron anomalies in Type IIb diamonds. The high stability of Fe^{3+} in high-P minerals (e.g., Frost et al., 2004; Kiseeva et al., 2018; Rohrbach et al., 2007) would drive Fe^{2+} to disproportionate ($3Fe^{2+} \rightarrow 2Fe^{3+} + Fe^{0}$), with Fe^{0} being exsolved as metal at >250 km depths (Frost et al., 2004; Rohrbach et al., 2007). Recent petrologic observations of natural samples, including metallic inclusions in diamonds (Anzolini et al., 2020; Smith et al., 2016) and the intergrowth of bridgmanite and metal in shock veins of meteorites (Bindi et al., 2020; Ghosh et al., 2021) strongly suggest the presence of metallic iron in the mantle created via the charge disproportionation reaction.

The carbon isotope composition of blue Type IIb diamonds, with low $\delta^{13}C$(−13‰) compared to mantle carbon (−5‰), is typically taken as further evidence of a subduction-related origin with a significant organic contribution ($\delta^{13}C = -25‰$) (Smith et al., 2018). However, other mechanisms may account for this isotopic signature, including high-T fractionation. An analysis of mantle-derived samples (Mikhail et al., 2014), high P–T experiments (Satish-Kumar et al., 2011), and calculations (J. Liu et al., 2019) reveals that iron–carbon melts become significantly depleted in ^{13}C when coexisting with other carbon-bearing phases, including diamond. Rayleigh distillation fractionation would progressively remove ^{13}C and concentrate incompatible B in iron–carbon melt. Metallic reservoirs in the mantle could therefore serve both as a ^{13}C-depleted and B-enriched source for Type IIb diamonds.

5. Conclusions

We use density functional theory molecular dynamics to predict the metal–silicate partitioning behavior of boron at pressures and temperatures of core formation. We find that boron becomes increasingly compatible with metal with increasing pressure–temperature, such that its behavior changes from lithophile to siderophile at conditions expected in magma oceans during core–mantle segregation. We illustrate this change in fundamental behavior qualitatively in two-phase simulations, and quantify metal–silicate partition coefficients ($D^{m/s}$) of boron by combining density functional theory molecular dynamics with thermodynamic integration calculations; $\log_{10}D^{m/s}$ increases from -0.8 ± 0.3 at low pressure–temperature (10 GPa and 3000 K) to 3.7 ± 0.1 at high pressure–temperature (130 GPa and 5000 K). We further predict that liquid silicates become enriched in the heavier boron isotope by >1‰ relative to liquid metal at conditions relevant to core formation. Our results provide evidence that metallic iron, present in the mantle and core, can serve as a major boron reservoir that may account for more than one half of Earth's overall boron inventory. This scenario offers an explanation for the anomalous elemental and isotopic boron signature in the deep Earth, alternative to mixing of recycled crust into the depleted mantle.

Data Availability Statement

The data reported in this paper can be freely downloaded in Figshare (https://doi.org/10.6084/m9.figshare.17086412.v3). All computations in this study were carried out using the Vienna ab initio simulation package (VASP) which is available for licensing at https://www.vasp.at/.

Acknowledgments
This work is supported by Deutsche Forschungsgemeinschaft (German Science Foundation, DFG) with grants STE1105/12-1 and STE1105/13-2 to G.S.N. Computations were performed at the Leibniz Supercomputing Center of the Bavarian Academy of Sciences and the Humanities, and the research center for scientific computing at the University of Bayreuth. Liang Yuan thanks the Alexander von Humboldt Foundation for financial support. Comments by Kate Kiseeva and an anonymous reviewer have significantly improved the manuscript. Open access funding enabled and organized by Projekt DEAL.

References

Alfè, D., Gillan, M. J., & Price, G. D. (2002). Composition and temperature of the Earth's core constrained by combining ab initio calculations and seismic data. *Earth and Planetary Science Letters*, *195*(1–2), 91–98. https://doi.org/10.1016/S0012-821X(01)00568-4

Anzolini, C., Marquardt, K., Stagno, V., Bindi, L., Frost, D. J., Pearson, D. G., et al. (2020). Evidence for complex iron oxides in the deep mantle from FeNi(Cu) inclusions in superdeep diamond. *Proceedings of the National Academy of Sciences of the United States of America*, *117*(35), 2108–21094. https://doi.org/10.1073/pnas.2004269117

Bermingham, K. R., & Walker, R. J. (2017). The ruthenium isotopic composition of the oceanic mantle. *Earth and Planetary Science Letters*, *474*, 466–473. https://doi.org/10.1016/j.epsl.2017.06.052

Bindi, L., Shim, S.-H., Sharp, T. G., & Xie, X. (2020). Evidence for the charge disproportionation of iron in extraterrestrial bridgmanite. *Science Advances*, *6*(2). https://doi.org/10.1126/sciadv.aay7893

Bouhifd, M. A., Jephcoat, A. P., Heber, V. S., & Kelley, S. P. (2013). Helium in Earth's early core. *Nature Geoscience*, *6*(11), 982–986. https://doi.org/10.1038/ngeo1959

Bourdon, B., Roskosz, M., & Hin, R. C. (2018). Isotope tracers of core formation. *Earth-Science Reviews*, *181*, 61–81. https://doi.org/10.1016/j.earscirev.2018.04.006

Brandon, A. D., Walker, R. J., Morgan, J. W., Norman, M. D., & Prichard, H. M. (1998). Coupled ^{186}Os and ^{187}Os evidence for core-mantle interaction. *Science*, *280*(5369), 1570–1573. https://doi.org/10.1126/science.280.5369.1570

Bull, A. L., McNamara, A. K., & Ritsema, J. (2009). Synthetic tomography of plume clusters and thermochemical piles. *Earth and Planetary Science Letters*, *278*(3–4), 152–162. https://doi.org/10.1016/j.epsl.2008.11.018

Cassé, M., Lehoucq, R., & Vangloni-Flam, E. (1995). Production and evolution of light elements in active star-forming regions. *Nature*, *373*(6512), 318–319. https://doi.org/10.1038/373318a0

Chaussidon, M., & Marty, B. (1995). Primitive boron isotope composition of the mantle. *Science*, *269*(5222), 383–386. https://doi.org/10.1126/science.269.5222.383

Chaussidon, M., & Robert, F. (1995). Nucleosynthesis of ^{11}B-rich boron in the pre-solar cloud recorded in meteoritic chondrules. *Nature*, *374*(6520), 337–339. https://doi.org/10.1038/374337a0

Chaussidon, M., & Robert, F. (1997). Comment on "Boron cosmochemistry II: Boron nucleosynthesis and condensation temperature" by M. Zhai. *Meteoritics & Planetary Sciences*, *32*(2), 321–323. https://doi.org/10.1111/j.1945-5100.1997.tb01270.x

Chemia, Z., Dolejš, D., & Steinle-Neumann, G. (2015). Thermal effects of variable material properties and metamorphic reactions in a three-component subducting slab. *Journal of Geophysical Research: Solid Earth*, *120*(10), 6823–6845. https://doi.org/10.1002/2015JB012080

Chou, C. L. (1978). Fractionation of siderophile elements in the Earth's upper mantle. *Proceedings of the 9th Lunar and Planetary Science Conference* (Vol. 1, pp. 219–230).

Dalou, C., Füri, E., Deligny, C., Piani, L., Caumon, M. C., Laumonier, M., et al. (2019). Redox control on nitrogen isotope fractionation during planetary core formation. *Proceedings of the National Academy of Sciences of the United States of America*, *116*(29), 14485–14494. https://doi.org/10.1073/pnas.1820719116

De Hoog, J. C. M., & Savov, I. P. (2018). Boron isotopes as a tracer of subduction zone processes. In *Advances in isotope geochemistry* (pp. 217–247). Springer.

Dorner, F., Sukurma, Z., Dellago, C., & Kresse, G. (2018). Melting Si: Beyond density functional theory. *Physical Review Letters*, *121*(19), 195701. https://doi.org/10.1103/PhysRevLett.121.195701

Fischer, R. A., Cottrell, E., Hauri, E., Lee, K. K. M., & Le Voyer, M. (2020). The carbon content of Earth and its core. *Proceedings of the National Academy of Sciences of the United States of America*, *117*(16), 8743–8749. https://doi.org/10.1073/pnas.1919930117

Fischer-Gödde, M., & Kleine, T. (2017). Ruthenium isotopic evidence for an inner Solar System origin of the late veneer. *Nature*, *541*(7638), 525–527. https://doi.org/10.1038/nature21045

Foster, G. L., Marschall, H., & Palmer, M. R. (2018). Boron isotope analysis of geological materials. In *Advances in isotope geochemistry* (pp. 13–31). Springer.

Frost, D. J., Liebske, C., Langenhorst, F. F., McCammon, C. A., Trønnes, R. G., & Rubie, D. C. (2004). Experimental evidence for the existence of iron-rich metal in the Earth's lower mantle. *Nature*, *428*(6981), 409–412. https://doi.org/10.1038/nature02413

Frost, D. J., & McCammon, C. A. (2008). The redox state of Earth's mantle. *Annual Review of Earth and Planetary Sciences*, *36*(1), 389–420. https://doi.org/10.1146/annurev.earth.36.031207.124322

Gaillou, E., Post, J. E., Rost, D., & Butler, J. E. (2012). Boron in natural type IIb blue diamonds: Chemical and spectroscopic measurements. *American Mineralogist*, *97*(1), 1–18. https://doi.org/10.2138/am.2012.3925

Ghosh, S., Tiwari, K., Miyahara, M., Rohrbach, A., Vollmer, C., Stagno, V., et al. (2021). Natural Fe-bearing aluminous bridgmanite in the Katol L6 chondrite. *Proceedings of the National Academy of Sciences*, *118*(40). https://doi.org/10.1073/pnas.2108736118

Gou, H., Dubrovinskaia, N., Bykova, E., Tsirlin, A. A., Kasinathan, D., Schnelle, W., et al. (2013). Discovery of a superhard iron tetraboride superconductor. *Physical Review Letters*, *111*(15), 157002. https://doi.org/10.1103/PhysRevLett.111.157002

Grew, E. S. (2017). Boron: From cosmic scarcity to 300 minerals. *Elements*, *13*(4), 225–229. https://doi.org/10.2138/gselements.13.4.225

Griffin, W. L., Gain, S. E. M., Saunders, M., Bindi, L., Alard, O., Toledo, V., & O'Reilly, S. Y. (2020). Parageneses of TiB_2 in corundum xenoliths from Mt. Carmel, Israel: Siderophile behavior of boron under reducing conditions. *American Mineralogist*, *105*(11), 1609–1621. https://doi.org/10.2138/am-2020-7375

Hartley, M. E., deHoog, J. C. M., & Shorttle, O. (2021). Boron isotopic signatures of melt inclusions from North Iceland reveal recycled material in the Icelandic mantle source. *Geochimica et Cosmochimica Acta*, *294*, 273–294. https://doi.org/10.1016/j.gca.2020.11.013

Hellmann, J. L., Hopp, T., Burkhardt, C., Becker, H., Fischer-Gödde, M., & Kleine, T. (2021). Tellurium isotope cosmochemistry: Implications for volatile fractionation in chondrite parent bodies and origin of the late veneer. *Geochimica et Cosmochimica Acta*, *309*, 313–328. https://doi.org/10.1016/j.gca.2021.06.038

Herzberg, C., Asimow, P. D., Ionov, D. A., Vidito, C., Jackson, M. G., & Geist, D. (2013). Nickel and helium evidence for melt above the core–mantle boundary. *Nature*, *493*(7432), 393–397. https://doi.org/10.1038/nature11771

Hin, R. C., Fitoussi, C., Schmidt, M. W., & Bourdon, B. (2014). Experimental determination of the Si isotope fractionation factor between liquid metal and liquid silicate. *Earth and Planetary Science Letters*, *387*, 55–66. https://doi.org/10.1016/j.epsl.2013.11.016

Hofmann, A. W., & White, W. M. (1982). Mantle plumes from ancient oceanic crust. *Earth and Planetary Science Letters*, *57*(2), 421–436. https://doi.org/10.1016/0012-821X(82)90161-3

Humayun, M. (2004). Geochemical evidence for excess iron in the mantle beneath Hawaii. *Science*, *306*(5693), 91–94. https://doi.org/10.1126/science.1101050

Jackson, M. G., Blichert-Toft, J., Halldórsson, S. A., Mundl-Petermeier, A., Bizimis, M., Kurz, M. D., et al. (2020). Ancient helium and tungsten isotopic signatures preserved in mantle domains least modified by crustal recycling. *Proceedings of the National Academy of Sciences of the United States of America*, *117*(49), 30993–31001. https://doi.org/10.1073/pnas.2009663117

Jin, Z., & Bose, M. (2019). New clues to ancient water on Itokawa. *Science Advances*, *5*(5). https://doi.org/10.1126/sciadv.aav8106

Kiseeva, E. S., Vasiukov, D. M., Wood, B. J., McCammon, C., Stachel, T., Bykov, M., et al. (2018). Oxidized iron in garnets from the mantle transition zone. *Nature Geoscience*, *11*(2), 144–147. https://doi.org/10.1038/s41561-017-0055-7

Kiseeva, E. S., & Wood, B. J. (2015). The effects of composition and temperature on chalcophile and lithophile element partitioning into magmatic sulphides. *Earth and Planetary Science Letters*, *424*, 280–294. https://doi.org/10.1016/J.EPSL.2015.05.012

Kobayashi, K., Tanaka, R., Moriguti, T., Shimizu, K., & Nakamura, E. (2004). Lithium, boron, and lead isotope systematics of glass inclusions in olivines from Hawaiian lavas: Evidence for recycled components in the Hawaiian plume. *Chemical Geology*, *212*(1–2), 143–161. https://doi.org/10.1016/j.chemgeo.2004.08.050

Kolmogorov, A. N., Shah, S., Margine, E. R., Bialon, A. F., Hammerschmidt, T., & Drautz, R. (2010). New superconducting and semiconducting Fe-B compounds predicted with an Ab initio evolutionary search. *Physical Review Letters*, *105*(21), 217003. https://doi.org/10.1103/PhysRevLett.105.217003

König, S., Lorand, J.-P., Luguet, A., & Graham Pearson, D. (2014). A non-primitive origin of near-chondritic S–Se–Te ratios in mantle peridotites; implications for the Earth's late accretionary history. *Earth and Planetary Science Letters*, *385*, 110–121. https://doi.org/10.1016/j.epsl.2013.10.036

Kowalski, P. M., & Jahn, S. (2011). Prediction of equilibrium Li isotope fractionation between minerals and aqueous solutions at high P and T: An efficient ab initio approach. *Geochimica et Cosmochimica Acta*, *75*(20), 6112–6123. https://doi.org/10.1016/j.gca.2011.07.039

Kresse, G., & Furthmüller, J. (1996). Efficient iterative schemes for ab initio total-energy calculations using a plane-wave basis set. *Physical Review B*, *54*(16), 11169–11186. https://doi.org/10.1103/PhysRevB.54.11169

Kresse, G., & Joubert, D. (1999). From ultrasoft pseudopotentials to the projector augmented-wave method. *Physical Review B*, *59*(3), 1758–1775. https://doi.org/10.1103/PhysRevB.59.1758

Leeman, W. P., & Sisson, V. B. (1996). Geochemistry of boron and its implications for crustal and mantle processes. *Reviews in Mineralogy*, *33*, 644–707. https://doi.org/10.1515/9781501509223-014

Liu, J., Wang, W., Yang, H., Wu, Z., Hu, M. Y., Zhao, J., et al. (2019). Carbon isotopic signatures of super-deep diamonds mediated by iron redox chemistry. *Geochemical Perspectives Letters*, *10*, 51–55. https://doi.org/10.7185/geochemlet.1915

Liu, M. C., & Chaussidon, M. (2018). The cosmochemistry of boron isotopes. In *Advances in isotope geochemistry* (pp. 273–289). Springer. https://doi.org/10.1007/978-3-319-64666-4_11

Lodders, K. (2003). Solar system abundances and condensation temperatures of the elements. *The Astrophysical Journal*, *591*(2), 1220–1247. https://doi.org/10.1086/375492

Marschall, H., & Jackson, M. (2020). Low recycling efficiency of boron into the deep mantle. In *EGU general assembly conference abstracts* (p. 10054).

Marschall, H., Wanless, V. D., Shimizu, N., Pogge von Strandmann, P. A. E., Elliott, T., & Monteleone, B. D. (2017). The boron and lithium isotopic composition of mid-ocean ridge basalts and the mantle. *Geochimica et Cosmochimica Acta*, *207*, 102–138. https://doi.org/10.1016/j.gca.2017.03.028

Marshall, E. W., Ranta, E., Halldórsson, S. A., Caracciolo, A., Bali, E., Jeon, H., et al. (2022). Boron isotope evidence for devolatilized and rehydrated recycled materials in the Icelandic mantle source. *Earth and Planetary Science Letters*, *577*, 117229. https://doi.org/10.1016/j.epsl.2021.117229

McCaig, A. M., Titarenko, S. S., Savov, I. P., Cliff, R. A., Banks, D., Boyce, A., & Agostini, S. (2018). No significant boron in the hydrated mantle of most subducting slabs. *Nature Communications*, *9*(1), 4602. https://doi.org/10.1038/s41467-018-07064-6

Mikhail, S., Guillermier, C., Franchi, I. A., Beard, A. D., Crispin, K., Verchovsky, A. B., et al. (2014). Empirical evidence for the fractionation of carbon isotopes between diamond and iron carbide from the Earth's mantle. *Geochemistry, Geophysics, Geosystems*, *15*(4), 855–866. https://doi.org/10.1002/2013GC005138

Mundl-Petermeier, A., Walker, R. J., Fischer, R. A., Lekic, V., Jackson, M. G., & Kurz, M. D. (2020). Anomalous ^{182}W in high ^{3}He/^{4}He ocean island basalts: Fingerprints of Earth's core? *Geochimica et Cosmochimica Acta*, *271*, 194–211. https://doi.org/10.1016/j.gca.2019.12.020

Ottolini, L., Laporte, D., Raffone, N., Devidal, J. L., & Fèvre, B. (2009). New experimental determination of Li and B partition coefficients during upper mantle partial melting. *Contributions to Mineralogy and Petrology*, *157*(3), 313–325. https://doi.org/10.1007/s00410-008-0336-7

Palme, H., Lodders, K., & Jones, A. (2013). Solar system abundances of the elements. *Treatise on Geochemistry* (2nd ed., Vol. 2, pp. 15–36). Elsevier. https://doi.org/10.1016/B978-0-08-095975-7.00118-2

Palme, H., & O'Neill, H. (2013). Cosmochemical estimates of mantle composition. *Treatise on Geochemistry* (2nd ed., Vol. 3, pp. 1–39). https://doi.org/10.1016/B978-0-08-095975-7.00201-1

Palmer, M. R. (2017). Boron cycling in subduction zones. *Elements*, *13*(4), 237–242. https://doi.org/10.2138/gselements.13.4.237

Palyanov, Y. N., Bataleva, Y. V., Sokol, A. G., Borzdov, Y. M., Kupriyanov, I. N., Reutsky, V. N., & Sobolev, N. V. (2013). Mantle-slab interaction and redox mechanism of diamond formation. *Proceedings of the National Academy of Sciences of the United States of America*, *110*(51), 20408–20413. https://doi.org/10.1073/pnas.1313340110

Palyanov, Y. N., Borzdov, Y. M., Khokhryakov, A. F., Bataleva, Y. V., & Kupriyanov, I. N. (2020). Effect of sulfur on diamond growth and morphology in metal-carbon systems. *CrystEngComm*, *22*(33), 5497–5508. https://doi.org/10.1039/d0ce00865f

Perdew, J. P., Burke, K., & Ernzerhof, M. (1996). Generalized gradient approximation made simple. *Physical Review Letters*, *77*(18), 3865–3868. https://doi.org/10.1103/PhysRevLett.77.3865

Piani, L., Marrocchi, Y., Rigaudier, T., Vacher, L. G., Thomassin, D., & Marty, B. (2020). Earth's water may have been inherited from material similar to enstatite chondrite meteorites. *Science*, *369*(6507), 1110–1113. https://doi.org/10.1126/science.aba1948

Prantzos, N. (2007). Stellar nucleosynthesis. In *Advances in astrobiology and biogeophysics* (pp. 1–43). Springer. https://doi.org/10.1007/978-3-540-33693-8_1

Prantzos, N. (2012). Production and evolution of Li, Be, and B isotopes in the Galaxy. *Astronomy and Astrophysics*, *542*, 67. https://doi.org/10.1051/0004-6361/201219043

Ramaty, R., Kozlovsky, B., & Lingenfelter, R. E. (1996). Light isotopes, extinct radioisotopes, and gamma-ray lines from low-energy cosmic-ray interactions. *The Astrophysical Journal*, *456*, 525. https://doi.org/10.1086/176677

Reeves, H., Fowler, W. A., & Hoyle, F. (1970). Galactic cosmic ray origin of Li, Be and B in stars. *Nature*, *226*(5247), 727–729. https://doi.org/10.1038/226727a0

Rizo, H., Andrault, D., Bennett, N. R., Humayun, M., Brandon, A., Vlastelic, I., et al. (2019). ^{182}W evidence for core-mantle interaction in the source of mantle plumes. *Geochemical Perspectives Letters*, *11*, 6–11. https://doi.org/10.7185/geochemlet.1917

Rohrbach, A., Ballhaus, C., Golla-Schindler, U., Ulmer, P., Kamenetsky, V. S., Kuzmin, D. V., et al. (2007). Metal saturation in the upper mantle. *Nature*, *449*(7161), 456–458. https://doi.org/10.1038/nature06183

Rubie, D. C., Frost, D. J., Mann, U., Asahara, Y., Nimmo, F., Tsuno, K., et al. (2011). Heterogeneous accretion, composition and core–mantle differentiation of the Earth. *Earth and Planetary Science Letters*, *301*(1–2), 31–42. https://doi.org/10.1016/J.EPSL.2010.11.030

Rudge, J. F., Kleine, T., & Bourdon, B. (2010). Broad bounds on Earth's accretion and core formation constrained by geochemical models. *Nature Geoscience*, *3*(6), 439–443. https://doi.org/10.1038/ngeo872

Satish-Kumar, M., So, H., Yoshino, T., Kato, M., & Hiroi, Y. (2011). Experimental determination of carbon isotope fractionation between iron carbide melt and carbon: ^{12}C-enriched carbon in the Earth's core? *Earth and Planetary Science Letters*, *310*(3–4), 340–348. https://doi.org/10.1016/j.epsl.2011.08.008

Schauble, E. A. (2004). Applying stable isotope fractionation theory to new systems. *Reviews in Mineralogy and Geochemistry*, *55*(1), 65–111. https://doi.org/10.2138/gsrmg.55.1.65

Shahar, A., Hillgren, V. J., Horan, M. F., Mesa-Garcia, J., Kaufman, L. A., & Mock, T. D. (2015). Sulfur-controlled iron isotope fractionation experiments of core formation in planetary bodies. *Geochimica et Cosmochimica Acta*, *150*, 253–264. https://doi.org/10.1016/j.gca.2014.08.011

Shahar, A., Ziegler, K., Young, E. D., Ricolleau, A., Schauble, E. A., & Fei, Y. (2009). Experimentally determined Si isotope fractionation between silicate and Fe metal and implications for Earth's core formation. *Earth and Planetary Science Letters*, *288*(1–2), 228–234. https://doi.org/10.1016/j.epsl.2009.09.025

Shaw, D. M., Higgins, M. D., Hinton, R. W., Truscott, M. G., & Middleton, T. A. (1988). Boron in chondritic meteorites. *Geochimica et Cosmochimica Acta*, *52*(9), 2311–2319. https://doi.org/10.1016/0016-7037(88)90133-0

Shearer, C. K., & Simon, S. B. (2017). Boron behavior during the evolution of the early solar system: The first 180 million years. *Elements*, *13*(4), 231–236. https://doi.org/10.2138/gselements.13.4.231

Siebert, J., Badro, J., Antonangeli, D., & Ryerson, F. J. (2012). Metal–silicate partitioning of Ni and Co in a deep magma ocean. *Earth and Planetary Science Letters*, *321–322*, 189–197. https://doi.org/10.1016/j.epsl.2012.01.013

Smith, E. M., Shirey, S. B., Nestola, F., Bullock, E. S., Wang, J., Richardson, S. H., & Wang, W. (2016). Large gem diamonds from metallic liquid in Earth's deep mantle. *Science*, *354*(6318), 1403–1405. https://doi.org/10.1126/science.aal1303

Smith, E. M., Shirey, S. B., Richardson, S. H., Nestola, F., Bullock, E. S., Wang, J., & Wang, W. (2018). Blue boron-bearing diamonds from Earth's lower mantle. *Nature*, *560*(7716), 84–87. https://doi.org/10.1038/s41586-018-0334-5

Sokol, A. G., Khokhryakov, A. F., Borzdov, Y. M., Kupriyanov, I. N., & Palyanov, Y. N. (2019). Solubility of carbon and nitrogen in a sulfur-bearing iron melt: Constraints for siderophile behavior at upper mantle conditions. *American Mineralogist*, *104*(12), 1857–1865. https://doi.org/10.2138/am-2019-7103

Steenstra, E. S., Trautner, V. T., Berndt, J., Klemme, S., & vanWestrenen, W. (2020). Trace element partitioning between sulfide-metal- and silicate melts at highly reduced conditions: Insights into the distribution of volatile elements during core formation in reduced bodies. *Icarus*, *335*, 113408. https://doi.org/10.1016/J.ICARUS.2019.113408

Syracuse, E. M., vanKeken, P. E., & Abers, G. A. (2010). The global range of subduction zone thermal models. *Physics of the Earth and Planetary Interiors*, *183*(1–2), 73–90. https://doi.org/10.1016/j.pepi.2010.02.004

Varas-Reus, M. I., König, S., Yierpan, A., Lorand, J. P., & Schoenberg, R. (2019). Selenium isotopes as tracers of a late volatile contribution to Earth from the outer Solar System. *Nature Geoscience*, *12*(9), 779–782. https://doi.org/10.1038/s41561-019-0414-7

Walowski, K. J., Kirstein, L. A., De Hoog, J. C. M., Elliott, T., Savov, I. P., & Jones, R. E., & EIMF. (2021). Boron recycling in the mantle: Evidence from a global comparison of ocean island basalts. *Geochimica et Cosmochimica Acta*, *302*, 83–100. https://doi.org/10.1016/j.gca.2021.03.017

Walowski, K. J., Kirstein, L. A., De Hoog, J. C. M., Elliott, T. R., Savov, I. P., & Jones, R. E. (2019). Investigating ocean island mantle source heterogeneity with boron isotopes in melt inclusions. *Earth and Planetary Science Letters*, *508*, 97–108. https://doi.org/10.1016/j.epsl.2018.12.005

Wang, Z., & Becker, H. (2013). Ratios of S, Se and Te in the silicate Earth require a volatile-rich late veneer. *Nature*, *499*(7458), 328–331. https://doi.org/10.1038/nature12285

Wilson, H. F., & Militzer, B. (2012). Solubility of water ice in metallic hydrogen: Consequences for core erosion in gas giant planets. *The Astrophysical Journal*, *745*(1), 54. https://doi.org/10.1088/0004-637X/745/1/54

Wohlers, A., & Wood, B. J. (2015). A Mercury-like component of early Earth yields uranium in the core and high mantle ^{142}Nd. *Nature*, *520*(7547), 337–340. https://doi.org/10.1038/nature14350

Wood, B. J., Halliday, A. N., & Rehkämper, M. (2010). Volatile accretion history of the Earth. *Nature*, *467*(7319), E6–E7. https://doi.org/10.1038/nature09484

Wood, B. J., & Kiseeva, E. S. (2015). Trace element partitioning into sulfide: How lithophile elements become chalcophile and vice versa. *American Mineralogist*, *100*(11–12), 2371–2379. https://doi.org/10.2138/am-2015-5358ccbyncnd

Wood, B. J., Smythe, D. J., & Harrison, T. (2019). The condensation temperatures of the elements: A reappraisal. *American Mineralogist*, *104*(6), 844–856. https://doi.org/10.2138/am-2019-6852CCBY

Worsham, E. A., & Kleine, T. (2021). Late accretionary history of Earth and Moon preserved in lunar impactites. *Science Advances*, *7*(44). https://doi.org/10.1126/sciadv.abh2837

Yierpan, A., König, S., Labidi, J., & Schoenberg, R. (2019). Selenium isotope and S-Se-Te elemental systematics along the Pacific-Antarctic ridge: Role of mantle processes. *Geochimica et Cosmochimica Acta*, *249*, 199–224. https://doi.org/10.1016/j.gca.2019.01.028

Zhai, M., & Shaw, D. M. (1994). Boron cosmochemistry. Part I: Boron in meteorites. *Meteoritics*, *29*(5), 607–615. https://doi.org/10.1111/j.1945-5100.1994.tb00773.x

References From the Supporting Information

Alfè, D. (2009). Temperature of the inner-core boundary of the Earth: Melting of iron at high pressure from first-principles coexistence simulations. *Physical Review B*, *79*(6), 060101. https://doi.org/10.1103/PhysRevB.79.060101

Allen, M. P., & Tildesley, D. J. (1989). *Computer simulation of liquids* (1st ed.). Oxford University Press. https://doi.org/10.1093/oso/9780198803195.001.0001

Bader, R. F. W. (1985). Atoms in molecules. *Accounts of Chemical Research*, *18*(1), 9–15. https://doi.org/10.1021/ar00109a003

Henkelman, G., Arnaldsson, A., & Jónsson, H. (2006). A fast and robust algorithm for Bader decomposition of charge density. *Computational Materials Science*, *36*(3), 354–360. https://doi.org/10.1016/j.commatsci.2005.04.010

He, X., Zhu, Y., Epstein, A., & Mo, Y. (2018). Statistical variances of diffusional properties from ab initio molecular dynamics simulations. *NPJ Computational Materials*, *4*(1), 1–9. https://doi.org/10.1038/s41524-018-0074-y

Lee, A. C., & Lee, S. K. (2020). Network polymerization and cation coordination environments in boron-bearing rhyolitic melts: Insights from ^{17}O, ^{11}B, and ^{27}Al solid-state NMR of sodium aluminoborosilicate glasses with varying boron content. *Geochimica et Cosmochimica Acta*, *268*, 325–347. https://doi.org/10.1016/j.gca.2019.10.010

Le Roux, S., & Jund, P. (2010). Ring statistics analysis of topological networks: New approach and application to amorphous GeS_2 and SiO_2 systems. *Computational Materials Science*, *49*(1), 70–83. https://doi.org/10.1016/j.commatsci.2010.04.023

Posysaev, S., Miroshnichenko, O., Alatalo, M., Le, D., & Rahman, T. S. (2019). Oxidation states of binary oxides from data analytics of the electronic structure. *Computational Materials Science*, *161*, 403–414. https://doi.org/10.1016/j.commatsci.2019.01.046

Schneider, C. A., Rasband, W. S., & Eliceiri, K. W. (2012). NIH image to ImageJ: 25 years of image analysis. *Nature Methods*, *9*(7), 671–675. https://doi.org/10.1038/nmeth.2089

Stukowski, A. (2010). Visualization and analysis of atomistic simulation data with OVITO-the Open Visualization Tool. *Modelling and Simulation in Materials Science and Engineering*, *18*(1), 015012. https://doi.org/10.1088/0965-0393/18/1/015012

Yuan, L., & Steinle-Neumann, G. (2020). Strong sequestration of hydrogen into the Earth's core during planetary differentiation. *Geophysical Research Letters*, *47*(15), e2020GL088303. https://doi.org/10.1029/2020GL088303

Yuan, L., Steinle-Neumann, G., & Suzuki, A. (2020). Structure and density of H_2O-rich Mg_2SiO_4 melts at high pressure from ab initio simulations. *Journal of Geophysical Research: Solid Earth*, *125*(10), e2020JB020365. https://doi.org/10.1029/2020JB020365

Zhang, Z., Csányi, G., & Alfè, D. (2020). Partitioning of sulfur between solid and liquid iron under Earth's core conditions: Constraints from atomistic simulations with machine learning potentials. *Geochimica et Cosmochimica Acta*, *291*, 5–18. https://doi.org/10.1016/j.gca.2020.03.028